


Dynamics and phases of nonunitary Floquet transverse-field Ising model

Lei Su¹, Aashish Clerk², and Ivar Martin^{1,3}

¹*Department of Physics, University of Chicago, Chicago, Illinois 60637, USA*

²*Pritzker School of Molecular Engineering, University of Chicago, Chicago, Illinois 60637, USA*

³*Materials Science Division, Argonne National Laboratory, Lemont, Illinois 60439, USA*

 (Received 28 July 2023; revised 23 October 2023; accepted 20 December 2023; published 31 January 2024)

Inspired by current research on measurement-induced quantum phase transitions, we analyze the nonunitary Floquet transverse-field Ising model with complex nearest-neighbor couplings and complex transverse fields. Unlike its unitary counterpart, the model shows a number of steady phases, stable to integrability-breaking perturbations. Some phases have robust edge modes and/or spatiotemporal long-range orders in the bulk. The transitions between the phases have extensive entanglement entropy, whose scaling with the system size depends on the number of the real quasiparticle modes in the spectrum at the transition. In particular, the volume-law scaling appears on some critical lines, protected by pseudo-Hermiticity. Both the scaling of entanglement entropy in steady states and the evolution after a quench are compatible with the non-Hermitian generalization of the quasiparticle picture of Calabrese and Cardy at least qualitatively.

DOI: [10.1103/PhysRevResearch.6.013131](https://doi.org/10.1103/PhysRevResearch.6.013131)

I. INTRODUCTION

Nonequilibrium quantum dynamics in many-body systems is an active area of research cutting across many different subfields of physics. While nontrivial dynamics can be generated in many different ways, there are two generic routes that are particularly attractive. The first is to induce dynamics by a periodic drive, the so-called Floquet approach. A wealth of recent work shows that many-body Floquet systems can exhibit novel phase transitions [1–5]. Realizing nontrivial quantum dynamics in interacting Floquet systems, however, requires extra ingredients that help suppress or completely avoid heating to an uninteresting infinite-temperature state [6–8]. In particular, the heating can be mitigated by introducing disorder which localizes energy via many-body localization (MBL) [1,4], or by adding external dissipation [9–11].

Another, seemingly distinct, route to novel nonequilibrium dynamics is to consider the evolution of a monitored many-body quantum system. By tuning the measurement rate, and considering an ensemble of quantum trajectories (each corresponding to a particular set of measurement outcomes), one can induce a novel class of phase transitions [12–14]. Instead of traditional phase transitions due to symmetry breaking, these measurement-induced phase transitions (MIPTs) do not have conventional order parameters, but instead are witnessed by entanglement properties and other quantum information-theoretical quantities [15,16]. First experimental evidence of such transitions has recently been reported [17,18].

In this work, we analyze a potentially even richer class of nonequilibrium many-body dynamics realized by combining time-periodic Floquet driving with effective nonunitary

evolution (which can be associated with monitoring of the quantum system). Our starting point is the archetypal Floquet transverse-field Ising model (TFIM), where a one-dimensional (1D) lattice of spins (described by Pauli operators X_j, Y_j, Z_j) evolves in each drive period according to the operator

$$U_F = e^{iJ \sum_j X_j X_{j+1}} e^{ih \sum_j Z_j}. \quad (1)$$

In the well-studied measurement-free case, J and h are real, and correspond respectively to uniform nearest-neighbor Ising interactions and transverse fields. For uniform J and h , if the initial state $|\Psi_0\rangle$ [Fig. 1(a)] is not a Floquet eigenstate, the system, in the long-time limit, may locally approach a periodic version of a generalized Gibbs ensemble [19]. On the other hand, if disorder is included, the model exhibits a number of unique nonequilibrium phases [1,4,20].

Instead of the unitary case specified above, here we consider what happens when the evolution operator U_F is made nonunitary by allowing both J and h to be complex. This is equivalent to adding measurement and postselection to our Floquet dynamics. To be concrete, suppose that each Z_j and each bond variable $X_j X_{j+1}$ are continuously monitored using a click-style measurement [21]. For each site j in the lattice there are two click detectors, A_j and B_j , with the probability of detector A generating a click in some time interval dt being controlled by the operator $\hat{A}_j = (1 \pm Z_j)/2$, and the probability of detector B clicking being controlled by the operator $\hat{B}_j = (1 \pm X_j X_{j+1})/2$. We specifically consider post-selected evolution on experimental runs where no clicks in any of the detectors are recorded. Using the standard theory of continuously monitored systems (see, e.g., Ref. [22]), one can show that the resulting evolution is controlled by a non-Hermitian Hamiltonian. The anti-Hermitian part is generated by the imaginary parts of J and h , which we denote β_J and β_h ; they correspond respectively to the strengths of

Published by the American Physical Society under the terms of the Creative Commons Attribution 4.0 International license. Further distribution of this work must maintain attribution to the author(s) and the published article's title, journal citation, and DOI.

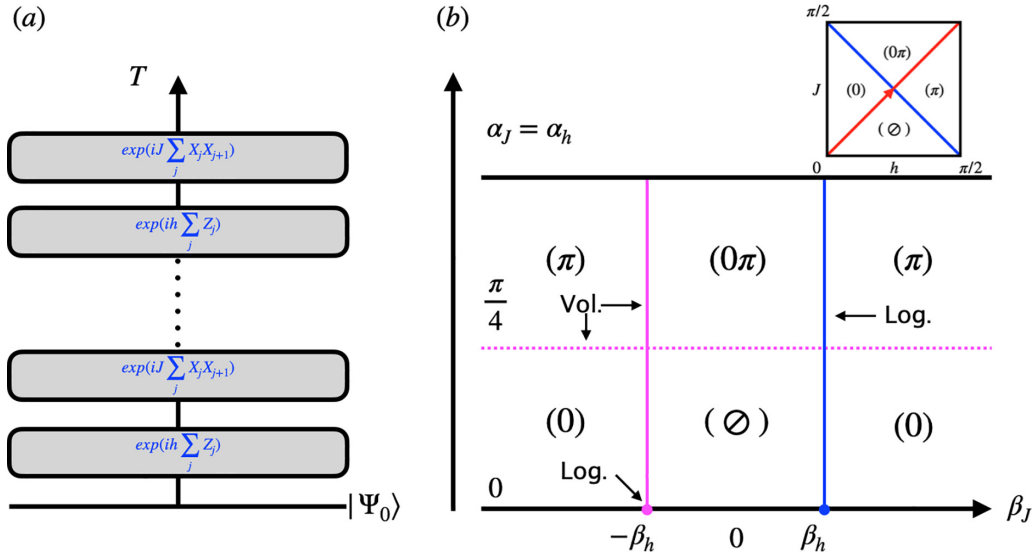


FIG. 1. (a) Floquet evolution in Eq. (1) of $|\Psi_0\rangle$. (b) Phase diagram of steady states for $\alpha_j = \alpha_h \equiv \alpha$. $\beta_h > 0$ is fixed and β_j is varied. It contains four different phases that satisfy an area law in entanglement entropy. The magenta boundaries (solid line, $\alpha_j = \alpha_h = \pi/4$, and dotted line, $\beta_j = -\beta_h$) represent a volume law while the blue solid line represents a logarithmic law. The critical points for $\alpha_j = \alpha_h = 0$ have a logarithmic law. The four phases are distinguished by the presence or absence of real 0- or π -edge modes in the spectrum with open boundary conditions. In particular, \emptyset means no edge modes. Inset: The phase diagram of the unitary Floquet model [1]; the real parts of the parameters used in the main panel sweep the red diagonal ($\alpha_h = \alpha_j$).

the A_j and B_j measurements. We note that special cases and particular aspects have been discussed in, e.g., Refs. [23–25].

The Floquet nonunitary TFIM allows us to study the interplay of Floquet driving and measurement-induced dynamics in the simpler setting where the evolution is deterministic (the specific postselection that we use eliminates the stochasticity inherent in quantum measurement). Despite the relative simplicity, we find a number of interesting effects:

(1) There is a rich variety of steady-state (long-time) phases, which can be characterized by the presence or absence of boundary Majorana modes in the fermionic language when open boundary conditions are used [see Fig. 1(b)].

(2) The entanglement entropies of the steady states can be understood in terms of the non-Hermitian quasiparticle picture, at least at the spectral level. In particular, non-area-law steady states appear when there are real modes in the spectrum. For example, this occurs on the boundaries between distinct phases, where there is an extensive growth in the steady-state entanglement entropy, with the growth being logarithmic or in some cases volume law. While some of the volume-law behaviors were previously noticed (when the nonunitary model is a spacetime dual to a unitary model [26–31]), we find new volume-law regimes that cannot be understood from the duality. Instead, we tie this new volume-law regime to the pseudo-Hermiticity of the non-Hermitian Floquet Hamiltonian. We show that the topological entanglement entropy that was employed to detect measurement-induced transitions in random quantum circuits [32] can also be used to locate some of these boundaries. This may provide an alternative angle to study Floquet non-Hermitian topological phases (see, e.g., Refs. [33,34]).

(3) The postselected measurement-induced dynamics we study allows one to directly stabilize dynamical phases, without the need for disorder, MBL, or additional engineered

dissipation. Importantly, this dynamics is robust against (at least) some integrability-breaking perturbations.

(4) Simple conformal field theory (CFT) with complex time can provide qualitative description of the entanglement entropy evolution, and the “central charge” of the Floquet criticality is parameter dependent.

In the rest of the paper, we substantiate and expand on these results as follows. In Sec. II, we describe the spin model and its fermionization as well as formulate the qualitative quasiparticle picture. Furthermore, we analyze the spectrum of the effective Hamiltonian with both periodic boundary conditions (PBCs) and open boundary conditions (OBCs) and study the evolution of entanglement entropy after a quantum quench. We then present the general phase diagram of steady states. In Sec. III, we report the detailed numerical analysis of entanglement entropy evolution and scaling, as well as topological entanglement entropy (TEE). We show that the entanglement entropy growth is consistent with the quasiparticle picture at least on the spectral level. Then, in Sec. IV, we discuss different quench dynamics of an open chain of spins in different phases. The effect of breaking the integrability is also briefly discussed. In Sec. V, we focus on the $J = h$ case (both complex) and compare the numerical results and the CFT results in both the continuous-time limit and the Floquet case. Finally, in Sec. VI, we summarize and mention some future directions. Some details are relegated to the Appendix.

II. MODEL

In our work, we consider a 1D chain of $1/2$ spins undergoing a time-periodic nonunitary evolution U_F described in Eq. (1). We start with an initial state $|\Psi_0\rangle$, e.g., a product state, and study the quench dynamics [see Fig. 1(a)]. We take $J \equiv \alpha_j + i\beta_j$ and $h \equiv \alpha_h + i\beta_h$ to be complex. Then U_F

induces a nonunitary Floquet evolution under non-Hermitian Hamiltonians $H_1 = J \sum_j X_j X_{j+1}$ and $H_2 = h \sum_j Z_j$. Since

$$U_F = e^{-\beta_J \sum_j X_j X_{j+1}} e^{i\alpha_J \sum_j X_j X_{j+1}} e^{-\beta_h \sum_j Z_j} e^{i\alpha_h \sum_j Z_j}, \quad (2)$$

U_F can be regarded as a unitary evolution interspersed with imaginary-time evolution. The imaginary-time evolution may be achieved by introducing couplings to ancillary spins (external to the circuit) that are being measured projectively [35]. As discussed in the Introduction, the imaginary-time evolution can also be associated with postselected measurement-induced dynamics.

Our study interpolates between and extends beyond several special cases that have been considered previously in the literature. If J and h are real, U_F gives a unitary evolution, and it corresponds to the noninteracting case of the kicked Ising model. Upon making a spacetime duality transformation, i.e., exchanging space and time, J and h become generally complex and satisfy $\alpha_J = \alpha_h = \pm\pi/4$. There are self-dual points at $|J| = |h| = \pi/4$ [26–29]. At these points, the dual of the original unitary circuit is also unitary, and such a circuit is called dual unitary. Many exact results can be derived using this defining property [26–29,36,37]. Away from self-dual points, however, the spacetime dual is no longer unitary, and corresponds to a non-Hermitian evolution. Naturally, the “evolution” along the spatial direction is not independent of the temporal evolution [30,31,38]. For instance, it has been shown that the entanglement entropy scaling (volume vs area law) of the output of the dual nonunitary circuit is directly related to the entanglement growth starting from an unentangled initial state in the original time direction (up to some boundary conditions) [31,39]. It was argued in Ref. [30] that the impediment to the entanglement growth in the presence of projective measurements is directly related to localization (area law) in the dual circuit.

When J and h are purely imaginary and small ($\beta_J > 0$ and $\beta_h < 0$), we recover the continuum limit, which was discussed in Ref. [40]. Our phase diagram includes an area-law-to-area-law phase transition via a logarithmic critical point, similar to the results in Ref. [41] (which were for a non-Floquet system). It was also found there that the phase diagram under the non-Hermitian evolution is smoothly connected to the phase diagram of a continuously monitored free fermion system. Related ideas have been explored also in Ref. [42], where MIPT was studied in a special model with an effective \mathcal{PT} -symmetric non-Hermitian Hamiltonian.

Although our model has a large parameter space [spanned by complex (J, h)], we will primarily focus here on the interesting case where $\alpha_J = \alpha_h$ (but β_J and β_h are general). Physically this corresponds to continuous monitoring of a critical unitary system [red line in the inset of Fig. 1(b)]. As we show, the continuous monitoring can drive the system into several distinct steady states as shown in the main panel of Fig. 1(b). We also note that while we focus on a particular set of postselected trajectories (the “no-click” trajectories), recent work on a related system suggests that the qualitative features here may also be characteristic of all trajectories [40].

A. The Jordan-Wigner transformation

To facilitate the analysis, we write the TFIM in terms of complex fermions by using the Jordan-Wigner transformation,

$$Z_j = 1 - 2c_j^\dagger c_j, \quad X_j X_{j+1} = (c_j^\dagger - c_j)(c_{j+1}^\dagger + c_{j+1}). \quad (3)$$

Furthermore, we define the real Majorana modes

$$a_{2j-1} = c_j + c_j^\dagger, \quad a_{2j} = i(c_j - c_j^\dagger), \quad (4)$$

which lead to further simplification,

$$U_F = U_{XX} U_Z = e^{-J \sum_{j=1}^L a_{2j} a_{2j+1}} e^{-h \sum_{j=1}^L a_{2j-1} a_{2j}}. \quad (5)$$

Here we have imposed the antiperiodic (periodic) boundary condition on fermions for the even (odd) fermion parity sector. In later discussions, we will also consider the case when OBCs are used. We can write

$$H_1 \equiv i \sum_{j=1}^L a_{2j} W'_{2j,2j+1} a_{2j+1} \quad (6)$$

and

$$H_2 \equiv i \sum_{j=1}^L a_{2j-1} W''_{2j-1,2j} a_{2j}, \quad (7)$$

where W' and W'' are $2L \times 2L$ matrices. Upon application of the Baker-Campbell-Hausdorff (BCH) formula, the bilinear structure of H_1 and H_2 leads to an effective bilinear Floquet Hamiltonian

$$H \equiv i \sum_{j,k=1}^{2L} a_j W_{j,k} a_k \quad (8)$$

with

$$e^{4W} = e^{4W'} e^{4W''}. \quad (9)$$

B. The quasiparticle picture

The simple bilinear form of Hamiltonian (8) implies the existence of noninteracting quasiparticle modes. The quasiparticle picture can be very useful for expressing the time dependence of wave functions as well as for interpreting the entanglement evolution after a quench [43,44]. Since the effective H is non-Hermitian, the quasiparticles are *not* canonical fermions [45,46].

If the non-Hermitian quadratic Hamiltonian H is diagonalizable, then $H = ADA^{-1}$ with diagonal D . The matrix A relates the canonical fermion modes a_j and the quasiparticles γ_k , and

$$H = \sum \epsilon_k \tilde{\gamma}_k^\dagger \gamma_k. \quad (10)$$

Here ϵ_k is in general complex and $\tilde{\gamma}_k^\dagger \neq \gamma_k^\dagger$. However, the anticommutation relations $\{\tilde{\gamma}_k^\dagger, \gamma_{k'}\} = \delta_{k,k'}$ are still satisfied. Let us denote $N_k \equiv \tilde{\gamma}_k^\dagger \gamma_k$. Then $[N_k, N_{k'}] = 0$ and $N_k^2 = N_k$. Therefore, we can conveniently use a nonorthonormal basis $|n_{k_1}, n_{k_2}, \dots, n_{k_L}\rangle$, such that $N_{k_i} |n_{k_1}, n_{k_2}, \dots, n_{k_L}\rangle = n_{k_i} |n_{k_1}, n_{k_2}, \dots, n_{k_L}\rangle$ where $n_k = 0, 1$. The expectation values

of N_k depend on time:

$$\langle N_k(t) \rangle = \frac{\langle \psi | e^{-it \sum_k \bar{\epsilon}_k \gamma_k^\dagger \tilde{\gamma}_k} \tilde{\gamma}_k^\dagger \gamma_k e^{it \sum_k \epsilon_k \tilde{\gamma}_k^\dagger \gamma_k} | \psi \rangle}{\langle \psi | \psi \rangle}. \quad (11)$$

Depending on the sign of $\text{Im}(\epsilon_k)$, $\langle N_k \rangle$ will evolve in time to either 0 or 1. In the long-time limit, only the real modes with $\text{Im}(\epsilon_k) = 0$ play a nontrivial role, similar to the purely real modes in unitary systems. Such (propagating) modes are expected to play an important role in distributing entanglement through a system starting from unentangled states [43]. In the thermodynamic limit, qualitatively, we expect that in the absence of real modes, the final entanglement scaling satisfies an area law. In contrast, for a finite density of real modes, the entanglement scaling will satisfy a volume law [43], whereas if we only have a finite number of real modes the entanglement scaling satisfies the logarithmic law.

There are a few points to be noted here. First, the system can be protected by the pseudo-Hermiticity [47] in some parameter regimes. Namely, there exists a Hermitian matrix η such that $\eta H \eta^{-1} = H^\dagger$. If a pseudo-Hermitian Hamiltonian H is diagonalizable, then it has an antilinear symmetry such as a \mathcal{PT} symmetry. The spectrum of H can be real if the antilinear symmetry is not spontaneously broken. Second, the real eigenmodes and the complex eigenmodes are not necessarily orthogonal, which could affect the quasiparticle picture of entanglement spreading. Nevertheless, we find that the heuristic non-Hermitian quasiparticle picture described above properly accounts for our numerical results. Similar discussion of the Su-Schrieffer-Heeger model can be found in Ref. [48], where it was found that the spectrum is dictated by the \mathcal{PT} symmetry and that the entanglement scaling also depends on the (partial) reality of the spectrum (see also Refs. [49–53]).

C. The spectrum

To obtain basic insights into our model, we first consider the spectrum of the problem. For PBCs, we identify regimes where the system has pseudo-Hermiticity symmetry, which has profound implications for the phase diagram. For PBCs, we find different localized edge Majorana mode configurations that correspond to different phases.

1. Periodic boundary condition: Continuous-time limit

Let us first consider the case $|J| = |h| \rightarrow 0$; then

$$\begin{aligned} U_F &\approx e^{iJ \sum_j X_j X_{j+1} + ih \sum_j Z_j} \\ &= e^{iJ \sum_j (c_j^\dagger - c_j)(c_{j+1}^\dagger + c_{j+1}) + ih \sum_j (1 - 2c_j^\dagger c_j)}. \end{aligned} \quad (12)$$

Diagonalizing the Hamiltonian in k space gives us the eigenvalues

$$\lambda_{1,2} = \pm 2\sqrt{h^2 - 2hJ \cos(k) + J^2}. \quad (13)$$

Importantly, it is possible for $\lambda_{1,2}$ to be real even for complex J and h . In those cases, the real modes behave similarly to the Hermitian case and may contribute to a non-area-law behavior in the steady-state entanglement entropy [43]. We now consider these special cases.

If $J = h$, then $\lambda_{1,2} = \pm 4J |\sin(k/2)|$. Therefore, for complex $J = h$ with small absolute values, at $k = 0$ we have $\lambda_{1,2} = 0$. The quasiparticle picture suggests that the steady

state will have a logarithmic-law behavior in entanglement entropy. This is not surprising because all modes but the zero mode will either decay or grow and will not contribute to the entanglement entropy.

If $J = \alpha + i\beta$ and $h = \alpha - i\beta$, then $\lambda_{1,2} = \pm 2\sqrt{2}\sqrt{\alpha^2 - \beta^2 - (\alpha^2 + \beta^2) \cos k}$. For a given k , the modes are either complex conjugates of one another or purely real. The condition $\cos k = (\alpha^2 - \beta^2)/(\beta^2 + \alpha^2)$ determines the exceptional points in the k space where the eigenvectors coalesce to $(-1, 1)/\sqrt{2}$. The existence of real modes and/or complex conjugate pairs is not a coincidence: For these parameters, it is protected by the pseudo-Hermiticity. In fact, if we write the Hamiltonian in Eq. (12) in the k space, for each 2×2 H_k , η is explicitly given by

$$\eta = \begin{pmatrix} 1 & \frac{\beta}{\alpha} \cot\left(\frac{k}{2}\right) \\ \frac{\beta}{\alpha} \cot\left(\frac{k}{2}\right) & 1 \end{pmatrix}. \quad (14)$$

Note that for generic complex J and h , there is no \mathcal{PT} or pseudo-Hermiticity symmetry to protect the reality of the spectrum, unlike in Refs. [42,48]. The pseudo-Hermiticity is important because it allows for the partially real spectrum, with the real modes generating a steady state with a volume law in entanglement entropy.

2. Periodic boundary conditions: General case

Now let us consider the Floquet unitary U_F of Eq. (1) for general parameter values. The spectrum is given by [30]

$$\epsilon_k = \pm \sqrt{-w_k^2}, \quad (15)$$

where

$$e^{w_k} = \frac{x}{4} \pm \sqrt{\left(\frac{x}{4}\right)^2 - 1} \quad (16)$$

with $x = 2(1 + \cos k) \cos(2h - 2J) + 2(1 - \cos k) \cos(2h + 2J)$. Similar to the continuous-time limit, a real zero mode exists at $k = 0$ for $J = h$. It is also easy to check that there are two cases that can lead to an extensive number of real modes: (1) $\alpha_J = \alpha_h = \pi/4 \pmod{\pi/2}$ (dual to the unitary case) and (2) $\alpha_J = \alpha_h \neq 0 \pmod{\pi/2}$, $\beta_J = -\beta_h$ (or $\alpha_J = -\alpha_h \neq 0 \pmod{\pi/2}$, $\beta_J = \beta_h$ in the spacetime dual). The spacetime duality is implemented by exchanging time and space coordinates [26,27,30]. In particular, for U_F , the spacetime dual has the form

$$\tilde{U}_F = e^{iJ' \sum_j X_j X_{\tau j+1}} e^{ih' \sum_j Z_{\tau j}} \quad (17)$$

up to some boundary terms. Here $J' = -\frac{\pi}{4} - \frac{i}{2} \log \tan h$ and $h' = -\frac{\pi}{4} - \frac{i}{2} \log \tan J$. For real J and h , U_F is unitary, corresponding to the first case. Indeed, if $J = h = \frac{\pi}{4} \lambda$, then $J' = h' = -\frac{\pi}{4} + i\beta$ with $\beta = \frac{1}{2} \log(\tan(\frac{\pi}{4} \lambda))$. It is easy to check that real modes exist between $[0, 2\pi\lambda]$ because $\cos^{-1}\left(\frac{\cosh(4\beta)-1}{\cosh(4\beta)+3}\right) = 2\pi\lambda$. This case is protected by the pseudo-Hermiticity of the effective Hamiltonian (expressed in terms of complex fermions in the k space) with the η matrix given by $\eta = \sigma_x$. The second case is a natural extension of the continuous-time case we discussed in the previous section. It is still protected by pseudo-Hermiticity but the η matrix is more complicated. This extensive number of real modes

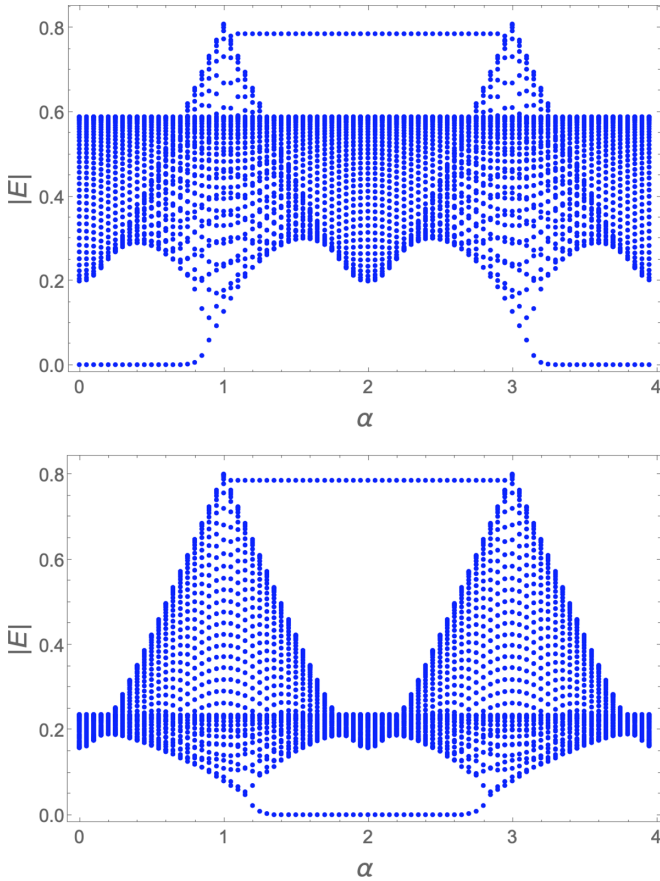


FIG. 2. Absolute values of the spectrum of the Hamiltonian H as a function of $\alpha = \alpha_J = \alpha_h$ when OBCs are used. $L = 40$. Top: $\beta_J = -1.0$, $\beta_h = 0.5$ (in units of $\pi/4$). Bottom: $\beta_J = -0.1$, $\beta_h = 0.5$ (in units of $\pi/4$).

will produce a volume law in the entanglement entropy in the steady state.

The cases with real modes define the position of the phase boundaries as shown in Fig. 1(b). Indeed, the quasiparticle picture implies that these real modes will not decay or grow and produce a non-area-law steady state. We will verify this numerically in the next section.

3. Open boundary conditions

If we use OBCs, it is easy to calculate the spectrum numerically in real space directly. The bulk of the spectrum is not very sensitive to the boundary conditions, but there can also be special edge modes: zero modes and π modes. In Fig. 2, we show the absolute value of the spectrum as we tune $\alpha = \alpha_J = \alpha_h$. We can check that these edge-mode energies are real. Because of the reflection symmetry, let us focus on the $0 \leq \alpha \leq \pi/2$ regime. In the upper panel, $\beta_J < -\beta_h$. When $\alpha \lesssim \pi/4$, the spectrum has zero edge modes, while for $\alpha \gtrsim \pi/4$, the spectrum has π edge modes. In the lower panel, $\beta_J > -\beta_h$. When $\alpha \lesssim \pi/4$, the spectrum has no edge modes, while when $\alpha \gtrsim \pi/4$, the spectrum has both zero and π modes. The presence or absence of the edge modes distinguishes different regimes in Fig. 1(b) and thus can be used to label the phases. Note that there is a strong finite-size effect when α is close to $\pi/4$. As the phase boundaries are

approached, the edge modes become non-normalizable for finite L . These edge modes are close relatives of those in the clean unitary case [54,55] as well as the Floquet-MBL unitary case [1]. They are the topological edge modes associated with Floquet symmetry-protected phases [56–58]. They retain real energies even when J and h become complex. We will see later in Sec. IV that these modes are good indicators of different dynamical behaviors after a quantum quench.

D. Evolution and steady states

Having established basic spectral features of our model, we now turn to the dynamics in a quench protocol where we start the system in a fermionic Gaussian state and let it evolve under U_F . The Floquet Hamiltonian H [Eq. (8)] has the following form in terms of complex fermions:

$$H = \sum \xi_{ij} c_i^\dagger c_j + \Delta_{ij}^- c_i c_j + \Delta_{ij}^+ c_j^\dagger c_i^\dagger. \quad (18)$$

In general, $\Delta_{ij}^+ \neq (\Delta_{ij}^-)^*$. In terms of real Majorana fermions,

$$H = \sum H_{ij} a_i a_j, \quad (19)$$

and hence

$$H^\dagger = \sum \tilde{H}_{ij}^T a_i a_j. \quad (20)$$

We want to study the evolution of the states under this generally non-Hermitian Hamiltonian. Since the Hamiltonian is quadratic, a Gaussian state remains Gaussian. We can calculate the entanglement entropy as a function of time from the correlation function $C_{ij}(t) = \langle \psi(t) | a_i a_j | \psi(t) \rangle / \langle \psi(t) | \psi(t) \rangle$, where $|\psi(t)\rangle = \exp(-iHt) |\psi_0\rangle$ and $|\psi_0\rangle$ is the initial state. Under the nonunitary evolution,

$$\frac{dC}{dt} = i(-C^T \tilde{H}^T C + C^T \tilde{H} C + C H C^T - C H^T C^T). \quad (21)$$

Note that since we used the effective Floquet Hamiltonian, only the correlation functions at multiples of the periods correspond to those in the original system. The time evolution of C can be obtained by solving this equation numerically. If it is a continuous-time evolution, the steady state is approached when $dC/dt \rightarrow 0$. In the Floquet setting, the definition of a steady state can be weakened: $C(t + nT) = C(t)$ where n is a positive integer and T is a period also yields a steady state, even if $C(t + T) \neq C(t)$. This case corresponds to discrete time crystals that spontaneously break the discrete time translation symmetry.

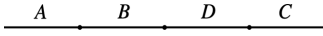
If we have a density matrix ρ of a total system comprised of subsystem A and subsystem B , we can obtain the reduced density matrix ρ_A by tracing out subsystem B : $\rho_A = \text{tr}_B \rho$. Then the von Neumann entanglement entropy is defined as $S_A = -\text{tr}[\rho_A \ln \rho_A]$. For the free fermion system, it can be evaluated directly using $C'_{ij} \equiv C_{ij} - \delta_{ij}$ [43]:

$$S_A = -\text{tr} \left[\frac{1 - C'_A}{2} \ln \frac{1 - C'_A}{2} + \frac{1 + C'_A}{2} \ln \frac{1 + C'_A}{2} \right], \quad (22)$$

where C'_A is C'_{ij} with i, j restricted in A . If all eigenvalues of C'_A are denoted as $\{\pm v_i\}$, we have

$$S_A = -\sum \left[\frac{1 - v_i}{2} \ln \frac{1 - v_i}{2} + \frac{1 + v_i}{2} \ln \frac{1 + v_i}{2} \right]. \quad (23)$$

In the case of OBCs, we will also be interested in a generalized TEE, which can be obtained from partitioning the one-dimensional system into four segments as follows:



Then TEE is defined as [32,40,59,60]

$$S_{\text{top}} = S_{AB} + S_{BC} - S_B - S_{ABC}. \quad (24)$$

This TEE was designed to detect ground-state topological transitions. As we will see in the next section, it can also be used to identify certain transitions in the steady state of our nonunitary Floquet system.

E. Phase diagram

We now briefly summarize the main features in the phase diagram of steady states shown in Fig. 1. The phase diagram can be determined easily by studying the spectra of the Hamiltonian H in Eq. (8). It depends on the relative magnitude of β_J and β_h . The phases are demarcated by the lines $|\beta_J| = |\beta_h|$, and $\alpha = \pi/4$. When $\beta_J = -\beta_h$, the steady-state entanglement entropy satisfies the volume law; when $\beta_J = \beta_h$ the steady-state entanglement entropy satisfies the logarithmic law (see next section). The volume-law phase at $\alpha = \pi/4$ exists because the nonunitary circuit is dual to a unitary circuit, as was already remarked in Ref. [30], but also because it is protected by the pseudo-Hermiticity, just as in the case $\beta_J = -\beta_h$. The rest of the phase diagram has an area law. If OBCs are imposed, the non-Hermitian spectrum may contain different real-energy edge modes (zero or π Majorana modes). Different phases are labeled by the modes present within them: (\emptyset) region (no edge modes), (0) region (zero modes), (π) region (π modes), and (0π) region (both zero and π modes).

In this work, we focused on the $\alpha_J = \alpha_h$ plane on the entire complex manifold where volume-law critical lines can be found. While we have not exhaustively studied parameter regimes $\alpha_J \neq \alpha_h$, a few general comments can be made on differences that emerge in this more general case. If $\alpha_J \neq \alpha_h$, the area-law phases can become logarithmic-law phases depending on β_J and β_h . The transitions between area-law phases become transitions between area-law phases and logarithmic-law phases. These scaling laws are still compatible with the quasiparticle picture at least at the spectral level: If the spectrum of the effective Floquet Hamiltonian contains no real modes, then it has an area-law scaling; on the other hand, if the spectrum contains a few real modes, the scaling is logarithmic. The volume laws we discussed on critical lines are replaced with logarithmic laws (see, e.g., Ref. [25]). There is a critical line for $\alpha_J \neq \alpha_h$ that corresponds to the critical line for $\alpha_J = \alpha_h = \pi/4$ while the boundaries at $\beta_J = \pm\beta_h$ remain where they were. Within phases, the edge modes persist, and different quench dynamics with OBCs (discussed in Sec. IV) only weakly depend on the condition $\alpha_J = \alpha_h$. We leave this detailed discussion to future work.

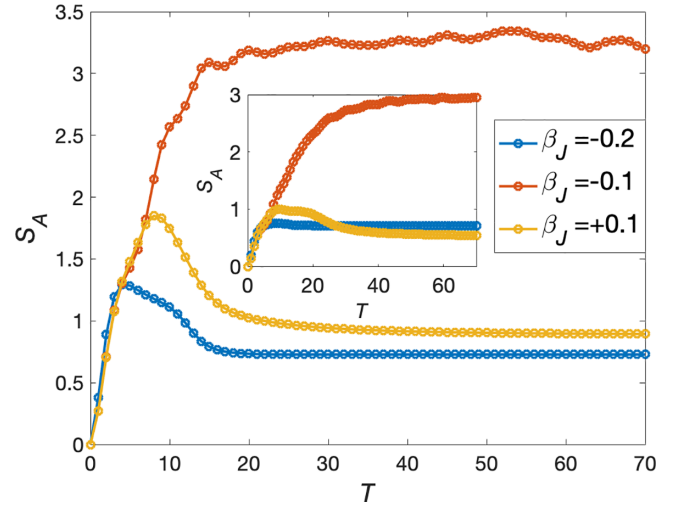


FIG. 3. Temporal evolution of entanglement entropy S_A with the PBCs. $\alpha = 0.2$, $\beta_h = 0.1$ (in units of $\pi/4$). $L_A = 8$ and $L_A/L = 1/20$. Inset: Evolution of S_A with OBCs. The subsystem A is chosen to be $[1, L_A]$. If the subsystem A is moved away from the boundary, the curves approach those with PBCs shown in the main panel.

III. ENTANGLEMENT ENTROPY EVOLUTION AND SCALING

In this section, we present the numerical results on the temporal evolution of entanglement entropy and its scaling in the steady states. For simplicity, we take L to be even and focus on the case in the initial state with odd (even) sites occupied and even (odd) sites empty. We will see the entanglement scaling is compatible with the quasiparticle picture for a quench problem. Namely, the steady state can have an area law, a logarithmic law, and a volume law, depending on whether the spectrum of the non-Hermitian Hamiltonian contains no real modes, a few real modes, or an extensive number of real modes, respectively. We also compute the TEE defined in Eq. (24) and use it to detect the phase transitions at $\beta_J = \pm\beta_h$.

A. $\alpha \neq \pi/4$

The phase diagram for this case can be seen in Fig. 1(b). We sample three representative points from the phase diagram: $\beta_J = -0.2, -0.1, 0.1$ while fixing $\alpha = 0.2$ and $\beta_h = 0.1$ (in units of $\pi/4$). The evolution of the entanglement entropy of subsystem A is shown in Fig. 3. The entanglement scaling in different phases is presented in Fig. 4 both on the linear scale and logarithmic scale.

If the system is in the area-law phase, the entanglement entropy first increases, and possibly drops before it saturates at long times. When $\beta_J = \beta_h$, the qualitative behavior of the evolution curve is similar and the system flows to a steady state with a logarithmic law. This pattern is general and shared by the CFT calculation to be discussed in Sec. V. When $\beta_J = -\beta_h$, the system approaches a volume law in the long-time limit. The evolution curve of S_A is similar to that of a unitary quench: It increases almost linearly at first and then saturates gradually after a time roughly proportional to L_A . The wiggly features are due to the finite-size effects: increasing the

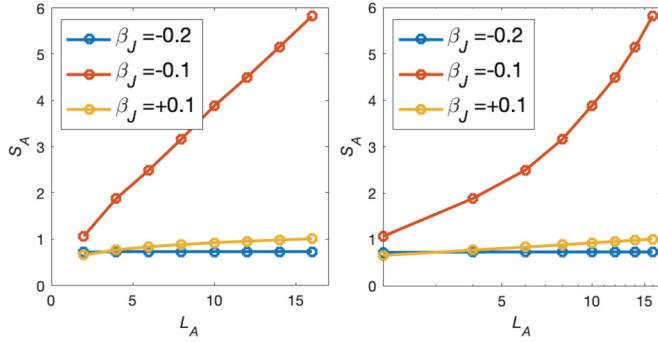


FIG. 4. Dependence of S_A on the subsystem size L_A . Linear (left) and logarithmic (right). $\alpha = 0.2$, $\beta_h = 0.1$ (in units of $\pi/4$). $L_A/L = 1/10$.

total system size reduces the entanglement revivals and thus smooths the curve.

In the above discussion, we imposed PBCs. If different boundary conditions are imposed, e.g., OBCs, the dynamical behavior can be slightly different. With OBCs, the entanglement entropy also depends on the location of subsystem A . If A is located deep in the bulk, then the entanglement entropy S_A becomes insensitive to the choice of boundary conditions and the curves approach those with PBCs (see the inset in Fig. 3). However, if A sits by the boundary, say, $[1, L_A]$, even though the qualitative features are the same, the saturated values of S_A are slightly different.

B. $\alpha = \pi/4$

When $\alpha = \pi/4$, the nonunitary circuit is dual to a unitary circuit. It sits on one of the critical lines of the phase diagram [Fig. 1(b)]. By resorting to the spacetime duality, it is easy to see that the steady state under the evolution of U_F has a volume-law scaling [dotted magenta line in Fig. 1(b)]. The volume law is compatible with the observation in Ref. [31] that an area-law steady state is ruled out (up to boundary conditions and fine tuning) for a nonunitary circuit that is dual to a unitary circuit which produces a non-area-law steady state. Previous works found that volume-law entanglement in a free-fermion chain is destroyed in the presence of arbitrarily weak measurements [61,62], and it was suggested in Ref. [30] that the volume law is symmetry protected by the unitarity of the unrotated circuit. However, as we have already mentioned, more generally, the volume-law phase is protected by the pseudo-Hermiticity of the effective Hamiltonian.

We also mentioned in Sec. II C that if $J = h = \alpha$ in the unitary circuit, then $J' = h' = -\frac{\pi}{4} + i\beta$ with $\beta = \frac{1}{2} \log(\tan(\alpha))$ and the real modes exist in the interval $[0, 8\alpha]$. In fact, we checked numerically that the entanglement entropy density S_A/L_A is almost linear in α if α is not too small (Fig. 5). Plotted together is the initial entanglement entropy growth rate. We see indeed that these two quantities are almost the same, which is not surprising because they are related by the spacetime duality [31,39] (up to boundary conditions and finite-size and finite-time effects).

We also present the time evolution of S_A of the nonunitary case with different $\beta = \beta_J = \beta_h$ in Fig. 6. We see that S_A increases almost linearly for small T and then saturates. As

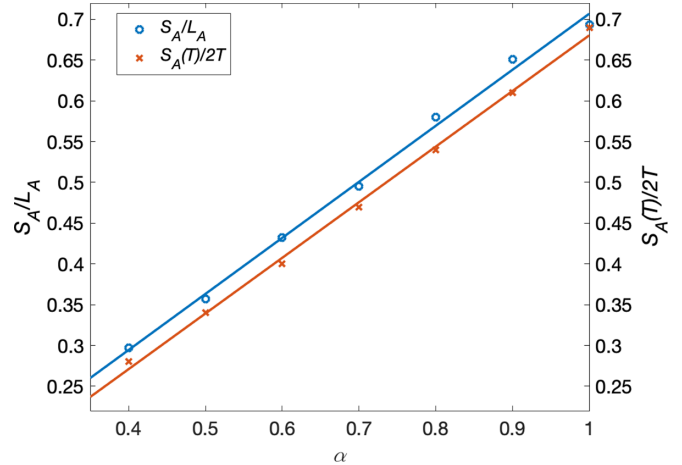


FIG. 5. Entanglement entropy density S_A/L_A (blue) and entanglement entropy early growth rate $S_A(T)/2T$ (red) as a function of $\alpha = J = h$ in the spacetime-dual model. $\beta_J = \beta_h = \log(\tan(\alpha))/(\pi/2)$ (in units of $\pi/4$). $L_A/L = 1/10$. Blue and red lines are the respective linear fits.

we increase β , since more modes become complex, S_A of the steady state decreases. Since S_A/L_A is almost linear in α , the dependence of S_A/L_A on β can be easily obtained by inverting the relation between β and α . In particular, if α is close to $\pi/4$, $\beta \approx \alpha - \pi/4$, and thus S_A/L_A is also linear in β for small β .

C. Topological entanglement entropy

We also compute the TEE [Eq. (24)] of different phases and show that it can always be used to detect the transition between (0) phase and the trivial (\emptyset) phases. In Fig. 7, TEE is shown for fixed α and β_h , and varying β_J . The TEE approaches zero for small $|\beta_J|$ and $\ln 2$ when $|\beta_J|$ is large. The curves associated with different sizes cross at a point where $\beta_{J0} \approx \beta_h$. The contribution to $\ln 2$ comes from a pair of Majorana modes ($2 \ln \sqrt{2}$). The finite-size scaling is presented

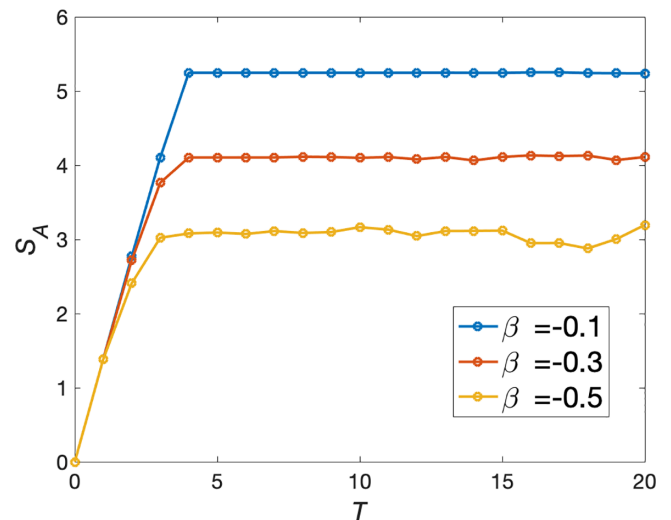


FIG. 6. Evolution of S_A for different $\beta = \beta_J = \beta_h$ and fixed $\alpha = 1$ (in units of $\pi/4$). $L_A = 8$, $L_A/L = 1/25$. PBCs are used.

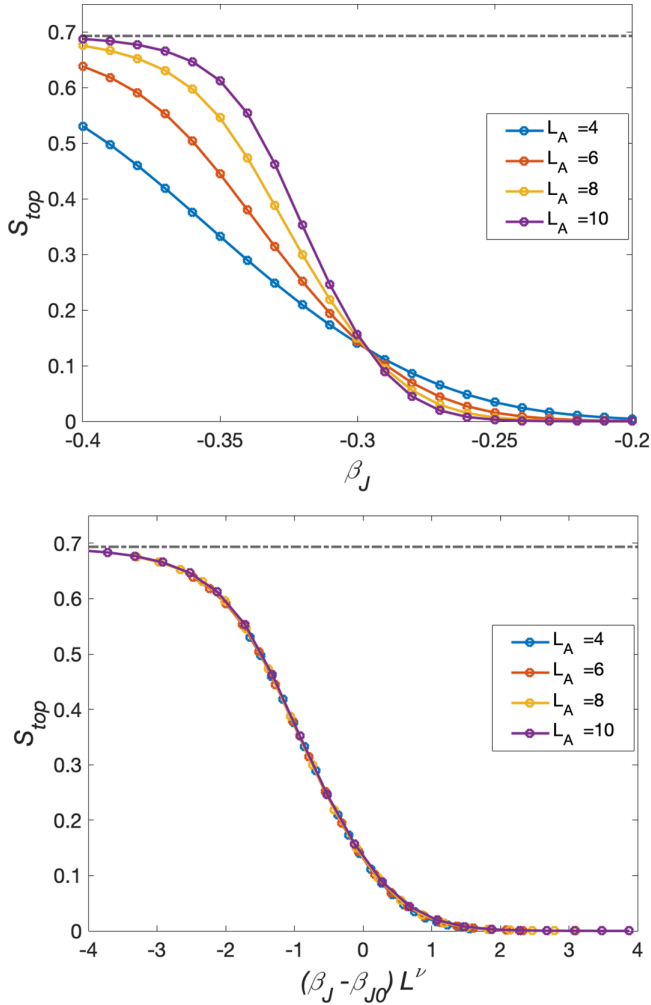


FIG. 7. (a) Topological phase transition between steady states, tuned by β_J and detected by TEE. $\alpha = 0.2$, $\beta_h = -0.3$ (in units of $\pi/4$). $L_A/L = 1/4$. OBCs are used. The dashed line marks $S_{\text{top}} = \ln 2$. (b) Scaling collapse of the data, obtained for $\beta_{J0} \approx \beta_h$ and $\nu \approx 1$.

in the lower panel by plotting S_{top} against $(\beta_J - \beta_{J0})L^\nu$. All data collapse almost perfectly onto a single curve. The critical exponent ν is determined to be approximately 1.

The TEE is also quantized to $\ln 2$ in the (π) phase as long as it stays away from the special line $\alpha = \pi/4$ where a phase transition occurs. We can interpret the (π) phase as alternation between two states in the (0) phase with opposite polarization. Then the TEE in the (π) phase at one instant is the same as that in the (0) phase. The topological information in the (0π) phase is more subtle, and we may need to construct a new quantity to extract it, which we leave for future work.

IV. QUANTUM QUENCH IN THE SPIN LANGUAGE

We have shown that zero modes and/or π modes exist in the fermionic language if OBCs are imposed (see Fig. 2), the same as in the unitary case [54,55]. Different combinations of edge modes are expected to be associated with different evolutions of many-body states. In this section we summarize the results on the time evolution obtained directly in the spin

language, starting from some random initial states (not close to Floquet eigenstates). We find four types of evolution corresponding to different phases in Fig. 1(b):

(i) In the trivial phase (\emptyset) , both $\langle S_x^i \rangle \rightarrow 0$ for all sites and $\langle S_x^i S_x^N \rangle \rightarrow 0$, where N is the total size, after a few drive periods [Fig. 8(a1)].

(ii) There are two regions in the phase diagram with zero modes (0) . If $\beta_J < -\beta_h$, for a small system, $\langle S_x^i \rangle$ of the state rapidly drops to zero while $\langle S_x^i S_x^N \rangle$ stays finite. For a small system, the final state has a large overlap with the Greenberger-Horne-Zeilinger state, $(|\uparrow\rangle^{\otimes L} + |\downarrow\rangle^{\otimes L})/\sqrt{2}$ (though it is very sensitive to integrability-breaking terms). Increasing the size slows down the initial decay of $\langle S_x^i \rangle$. In the thermodynamic limit, both $\langle S_x^i \rangle$ and $\langle S_x^i S_x^N \rangle$ should stabilize to a finite value, meaning that the steady state breaks the spin-flip \mathbb{Z}_2 symmetry [Fig. 8(b1)]. If $\beta_J > \beta_h$, the steady state is an antiferromagnet instead of a ferromagnet.

(iii) In the phases with a π mode (π) , the situation is similar to the one with the zero mode, except that the spins keep flipping, breaking the \mathbb{Z}_2 time-translational symmetry [Fig. 8(c1)]. A typical evolution of $\langle S_x^i \rangle$ of different sizes is shown in Fig. 9(a). We expect that in the thermodynamic limit, the steady state is in a Floquet (discrete time-crystal) phase. Moreover, if $\beta_J > \beta_h$, the steady state also breaks the \mathbb{Z}_2 translational symmetry, corresponding to an antiferromagnet as opposed to the case $\beta_J < -\beta_h$ when it is a ferromagnet [Fig. 8(c1)].

(iv) In the phase with both zero modes and π modes (0π) , the spins in the bulk $\langle S_x^i \rangle$ and the spins near the edges behave differently as illustrated in Fig. 8(d1). We take the initial state as a product state of polarized spins. Bulk spin correlations $\lim_{|i-j| \gg 1} \langle S_x^i S_x^j \rangle$ drop to zero, in contrast to the phases with only zero or π modes. The steady states depend on β_J and β_h . Thus, the initial behavior of different initial states can be different. In general, the oscillating pattern can be observed but edge spins have larger amplitudes. We expect that the bulk spin amplitudes approach zero in the thermodynamic limit, while the edge oscillations persist.

In the above discussion, OBCs were used. The main features in the (0) phase and the (π) phase are basically unaffected if PBCs are used. This implies emergence of the long-range order in the bulk. However, the (0π) phase depends crucially on the boundary conditions: Since this phase is evidenced solely by the edge spin oscillations, this signature disappears if we use PBCs.

We next compare these different dynamics with those in the unitary case. To this end, we plot quench dynamics with different real parameters in Figs. 8(a2)–8(d2). The four panels correspond to the same combinations of edge modes as in the nonunitary case. In a clean system, we can see that the edge states are robust. These features can be attributed to the presence of (almost) strong edge modes [55,63,64]. However, the bulk flows to the “infinite-temperature” state very quickly (up to revivals due to the finite system size). In the magnetically ordered phases, (0) and (π) , physically this can be understood in terms of domain-wall dynamics: Domain walls can move freely in the absence of disorder, quickly destroying the bulk order; however, they cannot flip the edge spins, since that would lead to a change in the number of domain walls, and thus significantly change the quasienergy. The situation is

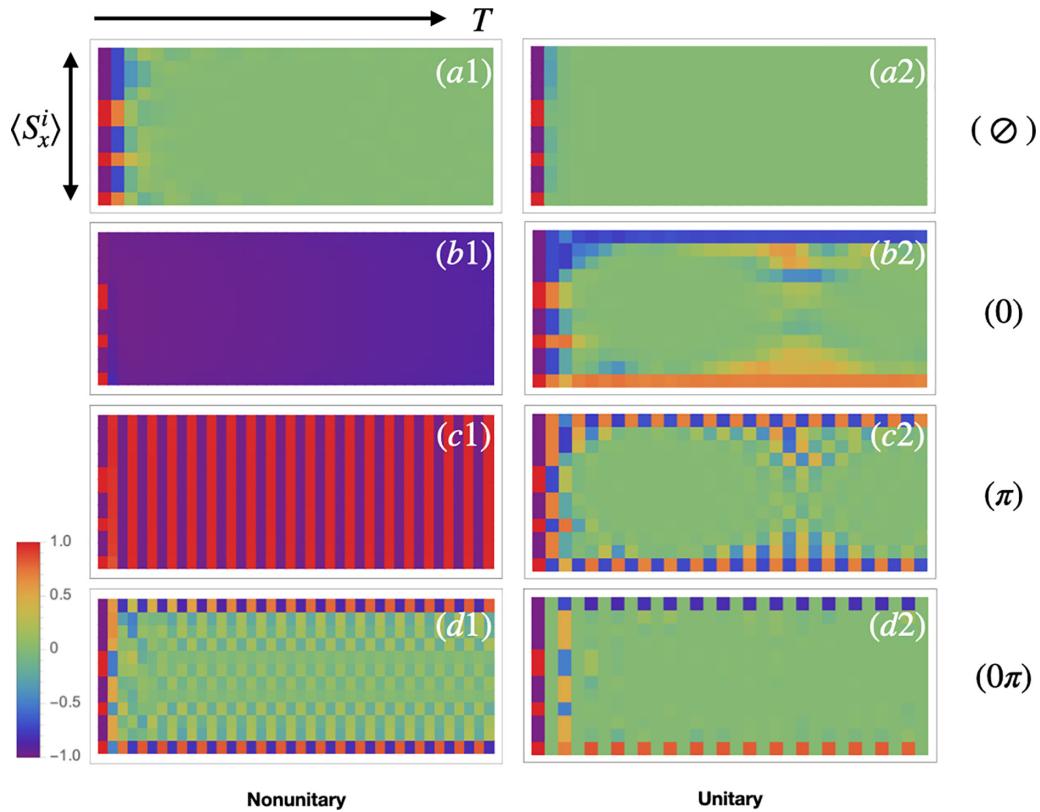


FIG. 8. Evolution of $\langle S_x^i \rangle$ in different phases (labeled along the right edge) in the nonunitary (left) and the unitary (right) case. Here, $i = 1, 2, \dots, L; L = 12$. In each panel, the spatial direction is vertical and the temporal direction is from left to right. The initial states are product states of spins (red, $|\uparrow\rangle$; purple, $|\downarrow\rangle$). (a1) $\alpha = 0.5, \beta_J = -0.5, \beta_h = 1.5$; (b1) $\alpha = 0.5, \beta_J = -1.5, \beta_h = 0.5$; (c1) $\alpha = 1.5, \beta_J = -1.5, \beta_h = 0.5$; (d1) $\alpha = 1.5, \beta_J = -0.1, \beta_h = 0.5$; (a2) $\alpha_J = 0.5, \alpha_h = 1.0$; (b2) $\alpha_J = 1.0, \alpha_h = 0.5$; (c2) $\alpha_J = 1.5, \alpha_h = 1.0$; (d2) $\alpha_J = 1.5, \alpha_h = 1.0$. All parameters are in units of $\pi/4$.

very different from the system with disorder (MBL regime) [1], where there are four different Floquet-MBL phases, each characterized by a unique eigenstate order. Apparently, comparing the figures on the left and on the right in Fig. 8, we find that the impact of imaginary parts of J and h is significant. In particular, the long-range bulk orders cannot be stabilized without the imaginary parts, i.e., measurements.

Since the TFIM is integrable, the steady states may depend on the initial states. Indeed, we see that if we start with

some special initial states, say, with $\sum_i \langle S_x^i \rangle = 0$, the quench dynamics can have a different behavior. One example in the (π) phase is given in Fig. 10(a) where the initial state is the antiferromagnetic state. This state has no overlap with the ferromagnetic (π) steady state [see Fig. 8(b1)] and as a result becomes featureless very quickly. However, if we add a small longitudinal field $K \sum_j X_j$ to break the integrability,

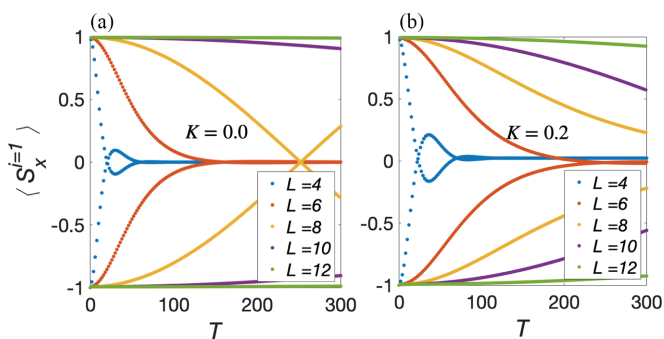


FIG. 9. Size dependence of $\langle S_x^{i=1} \rangle$ in the (π) phase. $\alpha = 1.5, \beta_J = -1.5, \beta_h = 0.5$ (in units of $\pi/4$). (a) Without integrability-breaking $K = 0.0$. (b) With integrability-breaking $K = 0.2$ (in units of $\pi/4$). The initial state is $|\downarrow \dots \downarrow\rangle$.

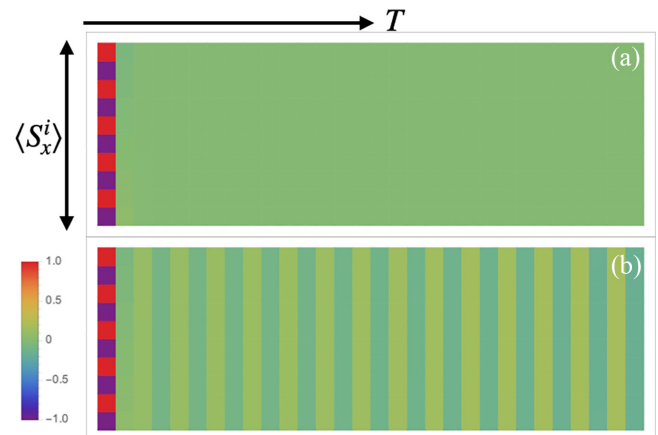


FIG. 10. Effect of the integrability-breaking term $K \sum_j X_j$ for a special initial (antiferromagnetic) state. (a) $K = 0.0$, (b) $K = 0.2$. $\alpha = 1.5, \beta_J = -1.5, \beta_h = 0.5$ (in units of $\pi/4$).

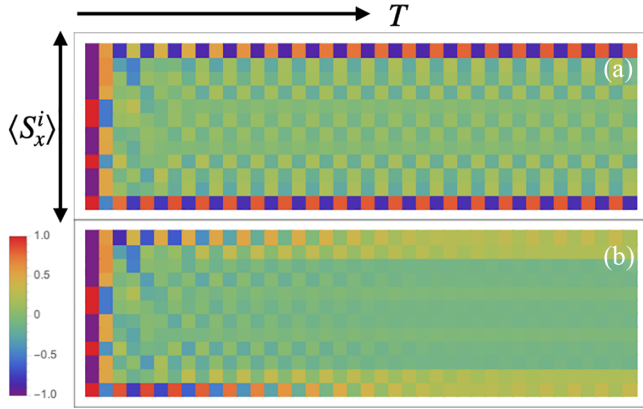


FIG. 11. Effect of the integrability-breaking term $K \sum_j X_j$ in the (0π) phase. (a) $K = 0.0$, (b) $K = 0.2$. $\alpha = 1.5$, $\beta_J = -0.1$, $\beta_h = 0.5$ (in units of $\pi/4$).

the steady state reminiscent of Fig. 8(b1) above reemerges [Fig. 10(b)].

We also studied the effect of the same integrability-breaking term $K \sum_j X_j$ on dynamics. The dependence of the evolution on the system size in the (π) phase when $K \neq 0$ is shown in Fig. 9(b). As we can see, when we increase the system size, the decay rate drops rapidly to zero. A similar pattern in the (0) phase is observed. Thus we expect these phases to be stable in the thermodynamic limit under the small perturbation ($0 < K \ll 1$). As can be seen from Fig. 11, in the (0π) phase, a small K can polarize the spins, but the edge-bulk distinction survives for a long time. This observation suggests that the influence of almost strong edge modes remains beyond the unitary case discussed in Ref. [55]. It is interesting to compare this behavior with the observation in the Google simulation in Ref. [65], where they observed that the edge spins under the unitary U_F evolution, in contrast to bulk spins, are resilient to integrability- and symmetry-breaking effects and dephasing effects such as low-frequency noise.

Finally, note that $\alpha_J = \alpha_h$ is not necessary to obtain different dynamics regimes in the nonunitary case that we identified above. We also expect that the main features are robust against other non-Hermitian deformations.

V. CONFORMAL FIELD THEORY AT $J = h$

So far, our focus has been on the area-law phases as well as volume-law critical lines in the phase diagram shown in Fig. 1(b). Now let us shift attention to the critical line with a logarithmic law at $J = h$. In the unitary case, i.e., J and h are real, if $|J| = |h| \rightarrow 0$, U_F approaches that of the TFIM in the continuous-time limit. The critical point is the celebrated Ising critical point described by the Ising CFT and the quench problem is well studied [43,66]. It is interpretable using the quasiparticle picture [43]. In the general case, the critical line (stabilized by disorder or interactions) may be called Floquet quantum criticality [67]. In this section, we extend J and h to complex values and study the quench problem.

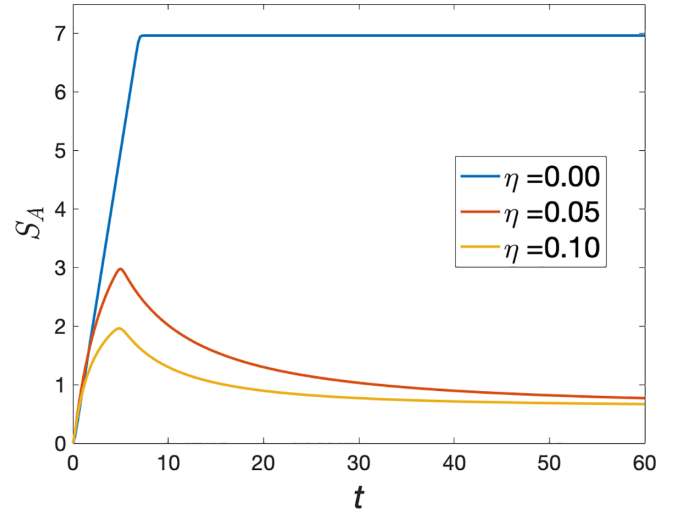


FIG. 12. Evolution of S_A in a CFT [Eq. (25)] with different η . $c = 1/2$, $\epsilon = 0.185$, $l = L_A = 10$.

A. Continuous-time limit

When $J = h$ and $|J| = |h| \rightarrow 0$, the qualitative behavior of the system is captured by the continuous-time limit where the dispersion is given by $\pm 4J |\sin(k/2)|$ [Eq. (13)]. For complex J and h , the dispersion is rotated to the complex plane in general. If we assume that the formalism developed by Calabrese and Cardy [43] can be generalized to this case, the quench problem can equivalently be described by $\exp(-i(1 - i\eta)tH_{\text{CFT}})$, where $\eta \geq 0$ quantifies the rotation. For more information, see the Appendix. Since $\exp(-i(1 - i\eta)tH_{\text{CFT}}) = \exp(-itH_{\text{CFT}}) \exp(-\eta tH_{\text{CFT}})$, the initial state first evolves by $\exp(-\eta tH_{\text{CFT}})$ then by the unitary operator $\exp(-itH_{\text{CFT}})$. Since $\exp(-\eta tH_{\text{CFT}})$ evolves the initial state to the ground state of H_{CFT} asymptotically, the long-time evolution approaches that of the ground state.

As discussed in the Appendix, the von Neumann entanglement entropy is

$$S_A(t) \equiv \left[-\frac{\partial}{\partial n} \text{tr} \rho_A^n(t) \right]_{n=1}, \quad (25)$$

with

$$\text{tr} \rho_A^n(t) \simeq \left(\frac{\pi}{2\tau_0} \right)^{2d_n} \left(\frac{\cosh(\pi l/2\tau_0) + \cosh(\pi t/\tau_0)}{8 \sinh(\pi l/4\tau_0)^2 \cosh^2(\pi t/2\tau_0)} \right)^{d_n}, \quad (26)$$

where $d_n = (c/12)(n - 1/n)$, c being the central charge, and $\tau_0 = \epsilon + \eta t$, ϵ being a regularization constant. In the derivation of the above equations, we have assumed $t, l \gg \tau_0$.

Typical evolutions of (normalized) von Neumann entanglement entropy S_A are depicted in Fig. 12. $\epsilon = 0.185$ is chosen such that if $\eta = 0$, S_A for $l = L_A$ saturates at the same value $S_A \sim \pi c l / 12 \epsilon$ of the Ising CFT ($c = 1/2$). When η becomes finite, S_A keeps increasing until $t \sim l/2$, then it starts to drop. In a closed system, the regularization ϵ affects both the initial growth rate and the saturation value of entanglement entropy. With dissipation η , ϵ becomes less important after some time: $t > \epsilon/\eta$. However, ϵ determines not only the initial maximum of S_A but also the ground-state entanglement entropy.

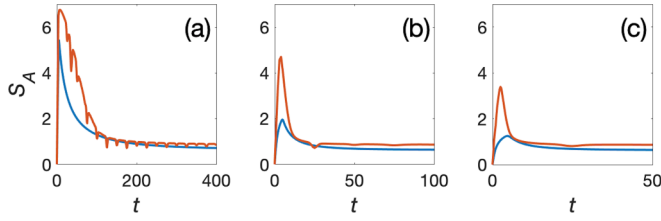


FIG. 13. Comparison of the evolution of S_A of a CFT and the numerical result of the nonunitary TFIM. The evolution in a CFT [Eq. (25)] with $c = 1/2$, $\epsilon = 0.185$, and $l = L_A = 10$ (blue). The evolution under U_F of the continuous complex TFIM [Eq. (12)] with $J = h = 1 - i\eta$, $L_A = 10$ and $L_A/L = 1/10$ (red). (a) $\eta = 0.01$, (b) $\eta = 0.10$, (c) $\eta = 0.20$. The oscillations are due to the finite-size effects.

The long-time limit depends on ϵ but not η because as we mentioned the state approaches the ground state. The larger η is, the faster the decaying rate is. In general, S_A can have a volume law before gradually approaching a logarithmic law at long times. The evolutions of S_A of the TFIM with continuous time and different η [Eq. (12)] are compared with those predicted by Eq. (25) in Fig. 13. We see that they match qualitatively.

Note that even though H_{CFT} is the critical Ising Hamiltonian in our main discussion, the formalism of Calabrese and Cardy [43] applies to general critical H_{CFT} . Thus, we expect the simple qualitative prediction from the CFT to be much more general. Also, as mentioned in Sec. III A, the pattern of the evolution of S_A , i.e., increasing first then decaying, is shared by the area-law phases. Similar features were observed in dissipative systems (see, e.g., Refs. [68,69]).

B. Floquet criticality

Since there is no phase transition until $\alpha_J = \alpha_h = \pi/4$, even though the preceding discussion was focused on the continuous-time limit, the evolution of entanglement entropy in Fig. 12 should qualitatively apply more broadly (i.e., for finite $J = h$). Once we move away from the continuous-time limit, the Floquet criticality [67] is no longer the canonical $c = 1/2$ Ising CFT. In Fig. 14(a), we fix the total system size $L = 100$ and plot S_A against different subsystem sizes L_A .

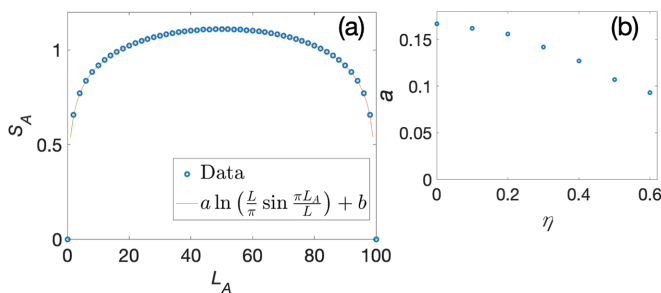


FIG. 14. (a) Subsystem dependence of S_A in a total system with $L = 100$ with fit in Eq. (27) using $J = h = 0.2 - 0.1i$ (in units of $\pi/4$). $a \approx 0.165$ and $b \approx 0.54$. (b) Fitting values of a as a function of η . $J = h = \eta i$ (in units of $\pi/4$).

Then the numerical data are fit by

$$a \ln \left(\frac{L}{\pi} \sin \frac{\pi L_A}{L} \right) + b \quad (27)$$

to extract the central charge [32,66]. In the continuous-time limit, $a = 1/6 = c/3$ since $c = 1/2$. In the Floquet setting, both a and b depend on $J = h$. The fitting in Eq. (27) applies as long as $\alpha = \alpha_J = \alpha_h$ is away from $\pi/4$, the critical line where the quench resembles that in the unitary case with an extensive number of real modes. For example, if $J = h = 0.2 - 0.1i$ (in units of $\pi/4$), we find $a \approx 0.165$ and $b \approx 0.54$. In general, the fit a depends on imaginary part β but not the real part α . Larger β leads to smaller a . In Fig. 14(b), we set $\alpha = 0$ and $\beta = \eta$, i.e., $J = h = \eta i$, and plot a for several values of η . We see that it decreases as a function of η .

VI. DISCUSSION

In this work, we have studied the nonunitary Floquet TFIM (kicked Ising model) with complex couplings and transverse fields. We analyzed the spectrum of the Floquet Hamiltonian in the fermionic language using the Jordan-Wigner transformation with both PBCs and OBCs, and used it to map out the phase diagram. For PBCs, we found that the spectrum may contain no real modes, a few real modes, or a finite density of real modes, the latter enabled by pseudo-Hermiticity of the Hamiltonian for special values of parameters. For OBCs, we found that real zero- and/or π -edge modes can exist in different phases. We presented the numerical result for the evolution of subsystem entanglement entropy after a quantum quench. In general, the entanglement entropy increases initially, then begins to drop, and eventually saturates to some steady-state value. The three just mentioned spectral cases lead to an area law, a logarithmic law, and a volume law of entanglement entropy in the steady state, respectively. The scaling behavior can be interpreted in terms of real-energy non-Hermitian quasiparticles being responsible for establishing entanglement (the initial entanglement peak can be attributed to complex-energy quasiparticles, which can lead to enhanced entanglement on the timescales of their lifetime). A quantized TEE exists if a zero mode or π mode exists. We also studied the quench dynamics of an open spin chain from a typical initial state and identified four types of dynamical behaviors corresponding to different edge-mode configurations. Compared to the clean unitary case, which generally lacks bulk long-range order, bulk order is stabilized by nonzero imaginary parts of J and h , i.e., measurements. Finally, we considered the case when $J = h$ and compared the numerical results in the continuous-time limit with the analytical result of a CFT by extending Calabrese and Cardy's formalism to complex time. They match qualitatively. Also, the effective central charge of the Floquet criticality was found to depend on $J = h$.

There are many promising future directions. First, there are many observables that can be used to study the nonunitary Floquet TFIM. In this work, we only computed entanglement entropy. As a matter of fact, we found mutual information has a similar behavior. It is also possible to compute other quantities such as entanglement negativity [70]. In particular, the general CFT formalism can also be generalized properly

to give us some insights into the evolution and the scaling of these quantities. In our work, we only discussed the non-Hermitian generalization of the quasiparticle picture at the spectral level; a quantitative check on the entanglement entropy growth as in Refs. [44,68,69] should be done. It is also interesting to see if more general topological quantities can be constructed to distinguish all four cases [so far we found that the $(0, \pi)$ phase is not clearly detected by TEE, in contrast to (0) and (π) phases]. In addition, the relation to the skin effects in the context of Floquet non-Hermitian topological phases [33,34] should be explored [71]. Also, we have focused on 1D spin chains. Some of our discussion for the 1D case can be easily generalized to higher dimensions.

Second, we have used non-Hermitian Hamiltonians as our starting point to study the effect of measurements by complexifying the coefficients. Complex J and h correspond to postselecting no-jump trajectories, with the jump operators $L_i = (1 \pm X_i X_{i+1})/2$ and $L_i = (1 \pm Z_i)/2$, respectively. There are many other types of measurements. We hope that the results of the simplified system can at least yield some insights into dynamical systems described by the stochastic Schrödinger equation where there are few or no postselections [40]. How more general continuously monitored systems behave deserves to be studied more closely (see, e.g., Refs. [41,61,69]). Whether different spin dynamics of a dissipative Floquet TFIM survive under a quench without postselection should be explored [10,40,65,72].

Third, there are many ways to extend the non-Hermitian Hamiltonian. Other physical effective Hamiltonians can be studied in a similar way. In this work we only briefly discussed the effect of the integrability-breaking term $\sum h_i X_i$ in the Hamiltonian. We can also include terms like $J_z \sum Z_i Z_{i+1}$ which after the Jordan-Wigner transformation is mapped to a density-density interaction [1]. Introducing long-range interactions is another direction with possible experimental relevance [10]. We know that introducing spatial disorder in the unitary case into such a system with a small J_z leads to MBL and stabilizes the Floquet phases [1,4]. How these systems respond to complexification of the coefficients is an interesting open question.

Lastly, several more general ideas discussed in this work deserve further investigation. For example, the partially real spectrum on some critical lines implies a spontaneous breaking of the antilinear symmetry associated with a diagonalizable pseudo-Hermitian Hamiltonian [47] as a function of momentum k (rather than some external control parameter). The effect of the existence of such an exceptional point in the k space on entanglement and purification transition should be further explored [42]. As another example, we noticed that positive or negative decay rates effectively lead to projective measurements in the momentum space. A general question is whether engineered dissipation can be used to construct interesting phases like topological phases [73–75].

ACKNOWLEDGMENTS

We thank R. Sahay for discussions. This material is based upon work supported by Laboratory Directed Research and Development (LDRD) funding from Argonne National Laboratory, provided by the Director, Office of Science, of the

U.S. Department of Energy under Contract No. DE-AC02-06CH11357.

APPENDIX: CONFORMAL FIELD THEORY WITH COMPLEX TIME

The evolution of entanglement entropy of a unitary critical system after a quantum quench is discussed in Refs. [43,66]. We discuss a minor generalization to a special critical non-Hermitian system by rotating the real time to the complex plane.

If H is the Hamiltonian of a CFT, then the non-Hermitian Hamiltonian $(1 - i\eta)H$ with $\eta > 0$ may be regarded as a critical Hamiltonian of the non-Hermitian system since the zero mode remains intact while other modes become complex. In our context, when $J = h = \alpha(1 - i\eta)$ and $|J| \ll 1$, the effective Hamiltonian is approximately described by that of a critical TFIM but with complex couplings. We assume that the CFT formalism is applicable to $(1 - i\eta)H$ and show that the CFT formalism yields results that are compatible with those in Ref. [69] qualitatively.

Suppose the system starts with the initial state $|\psi_0\rangle$ at $t = 0$ and then starts to evolve under $(1 - i\eta)H$. We first compute the density matrix

$$\begin{aligned} \langle \psi(x, t) | \rho_0 | \psi'(x', t) \rangle &= Z^{-1} \langle \psi(x) | e^{it(1+i\eta)H - \epsilon H} \rho_0 e^{-it(1-i\eta)H - \epsilon H} | \psi'(x') \rangle \\ &= Z^{-1} \langle \psi(x) | e^{-(t\eta + \epsilon - it)H} \rho_0 e^{-(t\eta + \epsilon + it)H} | \psi'(x') \rangle, \end{aligned} \quad (\text{A1})$$

where $\rho_0 = |\psi_0\rangle\langle\psi_0|$, $Z = \text{tr}[\rho_0 e^{-2(\epsilon + t\eta)H}]$, and a term ϵH has been added to make the quantity convergent.

Let us write $\tau_1 = \epsilon + t\eta + it$ and $\tau_2 = \epsilon + t\eta - it$; then the density matrix ρ can be represented as two path integrals: the first one starts with $\psi'(x', \tau)$ at $\tau = -\tau_1$ and ends with $\psi_0(x)$ at $\tau = 0$, and the second one starts with $\psi_0(x)$ at $\tau = 0$ and terminates with $\psi(x, \tau)$ at $\tau = \tau_2$. Divide the system (at $\tau = 0$) into region A and its complement B ; then the reduced density matrix ρ_A can be obtained by gluing $\psi_0(x)$ of the first integral with that of the second one at $\tau = 0$ for x inside region B . $\text{tr}\rho_A^n$ can be obtained by cyclic gluing:

$$\text{tr}\rho_A^n = Z_n(A)/Z^n, \quad (\text{A2})$$

where $Z_n(A)$ is the path integral on an n -sheet surface. Taking $n = 1$ and A to be the entire system, we have $Z_1 = Z$ and $\text{tr}\rho = 1$. The Rényi entropies are given by

$$S_A^{(n)} = \frac{1}{1-n} \text{tr}\rho_A^n, \quad (\text{A3})$$

and the von Neumann entanglement entropy by

$$S_A = -\frac{\partial}{\partial n} \text{tr}\rho_A^n \Big|_{n=1}. \quad (\text{A4})$$

To compute $\text{tr}\rho_A^n$, we make use of the conformal invariance and parametrize the strip with width $\tau = \tau_1 + \tau_2$ by the upper half plane of the complex plane via the conformal map $w = (2\tau_0/\pi) \log z$ with $\tau_0 = \epsilon + \eta t$. If the total length of A is l and the original end points of A sit at $-l/2$ and $l/2$, the images of these two branch points are $z_1 = \exp(-\pi l/4\tau_0) \exp(i\pi \tau_1/2\tau_0)$ and $z_2 = \exp(\pi l/4\tau_0) \exp(i\pi \tau_1/2\tau_0)$, respectively. Following

Ref. [43], $Z_n(A)/Z^n$ can be computed from the correlation function of the two branch point twist fields with scaling dimension $d_n = (c/12)(n - 1/n)$:

$$\text{tr}\rho_A^n(t) \simeq \tilde{\mathcal{F}}_n(x)c_n \left(\frac{\pi}{2\tau_0}\right)^{2d_n} \times \left(\frac{\cosh(\pi l/2\tau_0) + \cosh(\pi t/\tau_0)}{8 \sinh(\pi l/4\tau_0)^2 \cosh^2(\pi t/2\tau_0)}\right)^{d_n}, \quad (\text{A5})$$

where $\tilde{\mathcal{F}}_n(x)$ is a function that depends on the model and the boundary condition, x being the four-point ratio, and c_n are constants that cannot be determined with this method but $c_1 = 1$. If we are interested in asymptotic behaviors, e.g., $t, l \gg \tau_0$, $\tilde{\mathcal{F}}_n(x)$ is irrelevant and we can put it to be 1. After

some algebraic manipulations, we obtain

$$\text{tr}\rho_A^n(t) \simeq c_n \left(\frac{\pi}{2\tau_0}\right)^{2d_n} \left(\frac{e^{\pi l/2\tau_0} + e^{\pi t/\tau_0}}{e^{\pi l/2\tau_0} e^{\pi t/\tau_0}}\right)^{d_n}. \quad (\text{A6})$$

Note that since $\tau_0 = \epsilon + \eta t$, for $t, l \gg \tau_0$ to be satisfied, we require that $\eta \ll 1$ and $t \ll l/\eta$. We can normalize the entanglement entropy by subtracting $S_A(0)$ from $S_A(t)$. Using the approximation in Eq. (A6), we find that normalized entanglement entropy is given by

$$S_A(t) \simeq \frac{c}{3} \ln \left(\frac{\epsilon + \eta t}{\epsilon}\right) + \begin{cases} \frac{\pi c t}{6(\epsilon + \eta t)}, & \epsilon \ll t < l/2 \\ \frac{\pi c l}{12(\epsilon + \eta t)}, & l/2 < t \ll l/\eta. \end{cases} \quad (\text{A7})$$

If we take $l/2 < t < l/\eta$ and $t \rightarrow \infty$, $S_A(t)$ will saturate.

The derivation above can be generalized to Rényi entropies straightforwardly. In fact, Rényi entropies have similar behaviors as the von Neumann entanglement entropy.

-
- [1] V. Khemani, A. Lazarides, R. Moessner, and S. L. Sondhi, Phase structure of driven quantum systems, *Phys. Rev. Lett.* **116**, 250401 (2016).
- [2] D. V. Else, B. Bauer, and C. Nayak, Floquet time crystals, *Phys. Rev. Lett.* **117**, 090402 (2016).
- [3] C. W. von Keyserlingk, V. Khemani, and S. L. Sondhi, Absolute stability and spatiotemporal long-range order in Floquet systems, *Phys. Rev. B* **94**, 085112 (2016).
- [4] R. Moessner and S. L. Sondhi, Equilibration and order in quantum Floquet matter, *Nat. Phys.* **13**, 424 (2017).
- [5] F. Harper, R. Roy, M. S. Rudner, and S. Sondhi, Topology and broken symmetry in Floquet systems, *Annu. Rev. Condens. Matter Phys.* **11**, 345 (2020).
- [6] L. D'Alessio and M. Rigol, Long-time behavior of isolated periodically driven interacting lattice systems, *Phys. Rev. X* **4**, 041048 (2014).
- [7] A. Lazarides, A. Das, and R. Moessner, Equilibrium states of generic quantum systems subject to periodic driving, *Phys. Rev. E* **90**, 012110 (2014).
- [8] P. Ponte, A. Chandran, Z. Papić, and D. A. Abanin, Periodically driven ergodic and many-body localized quantum systems, *Ann. Phys.* **353**, 196 (2015).
- [9] H. Deghani, T. Oka, and A. Mitra, Dissipative Floquet topological systems, *Phys. Rev. B* **90**, 195429 (2014).
- [10] P. Sierant, G. Chiriaco, F. M. Surace, S. Sharma, X. Turkeshi, M. Dalmonte, R. Fazio, and G. Pagano, Dissipative Floquet dynamics: From steady state to measurement induced criticality in trapped-ion chains, *Quantum* **6**, 638 (2022).
- [11] T. Mori, Floquet states in open quantum systems, *Annu. Rev. Condens. Matter Phys.* **14**, 35 (2023).
- [12] Y. Li, X. Chen, and M. P. A. Fisher, Quantum Zeno effect and the many-body entanglement transition, *Phys. Rev. B* **98**, 205136 (2018).
- [13] B. Skinner, J. Ruhman, and A. Nahum, Measurement-induced phase transitions in the dynamics of entanglement, *Phys. Rev. X* **9**, 031009 (2019).
- [14] A. Chan, R. M. Nandkishore, M. Pretko, and G. Smith, Unitary-projective entanglement dynamics, *Phys. Rev. B* **99**, 224307 (2019).
- [15] A. C. Potter and R. Vasseur, Entanglement dynamics in hybrid quantum circuits, in *Entanglement in Spin Chains: From Theory to Quantum Technology Applications* (Springer, Berlin, 2022), pp. 211–249.
- [16] M. P. Fisher, V. Khemani, A. Nahum, and S. Vijay, Random quantum circuits, *Annu. Rev. Condens. Matter Phys.* **14**, 335 (2023).
- [17] C. Noel *et al.*, Measurement-induced quantum phases realized in a trapped-ion quantum computer, *Nat. Phys.* **18**, 760 (2022).
- [18] J. M. Koh, S.-N. Sun, M. Motta, and A. J. Minnich, Measurement-induced entanglement phase transition on a superconducting quantum processor with mid-circuit readout, *Nat. Phys.* **19**, 1314 (2023).
- [19] A. Lazarides, A. Das, and R. Moessner, Periodic thermodynamics of isolated quantum systems, *Phys. Rev. Lett.* **112**, 150401 (2014).
- [20] B. Bauer, T. Pereg-Barnea, T. Karzig, M.-T. Rieder, G. Refael, E. Berg, and Y. Oreg, Topologically protected braiding in a single wire using Floquet Majorana modes, *Phys. Rev. B* **100**, 041102(R) (2019).
- [21] X. Turkeshi, A. Biella, R. Fazio, M. Dalmonte, and M. Schiró, Measurement-induced entanglement transitions in the quantum Ising chain: From infinite to zero clicks, *Phys. Rev. B* **103**, 224210 (2021).
- [22] H. M. Wiseman and G. J. Milburn, *Quantum Measurement and Control* (Cambridge University Press, Cambridge, UK, 2009).
- [23] S. Basu, D. P. Arovas, S. Gopalakrishnan, C. A. Hooley, and V. Oganessian, Fisher zeros and persistent temporal oscillations in nonunitary quantum circuits, *Phys. Rev. Res.* **4**, 013018 (2022).
- [24] V. Ravindranath and X. Chen, Robust oscillations and edge modes in nonunitary Floquet systems, *Phys. Rev. Lett.* **130**, 230402 (2023).
- [25] E. Granet, C. Zhang, and H. Dreyer, Volume-law to area-law entanglement transition in a nonunitary periodic Gaussian circuit, *Phys. Rev. Lett.* **130**, 230401 (2023).
- [26] B. Bertini, P. Kos, and T. Prosen, Exact spectral form factor in a minimal model of many-body quantum chaos, *Phys. Rev. Lett.* **121**, 264101 (2018).

- [27] B. Bertini, P. Kos, and T. Prosen, Entanglement spreading in a minimal model of maximal many-body quantum chaos, *Phys. Rev. X* **9**, 021033 (2019).
- [28] B. Bertini, P. Kos, and T. Prosen, Exact correlation functions for dual-unitary lattice models in $1 + 1$ dimensions, *Phys. Rev. Lett.* **123**, 210601 (2019).
- [29] L. Piroli, B. Bertini, J. I. Cirac, and T. Prosen, Exact dynamics in dual-unitary quantum circuits, *Phys. Rev. B* **101**, 094304 (2020).
- [30] T.-C. Lu and T. Grover, Spacetime duality between localization transitions and measurement-induced transitions, *PRX Quantum* **2**, 040319 (2021).
- [31] M. Ippoliti, T. Rakovszky, and V. Khemani, Fractal, logarithmic, and volume-law entangled nonthermal steady states via spacetime duality, *Phys. Rev. X* **12**, 011045 (2022).
- [32] A. Lavasani, Y. Alavirad, and M. Barkeshli, Measurement-induced topological entanglement transitions in symmetric random quantum circuits, *Nat. Phys.* **17**, 342 (2021).
- [33] A. Banerjee, R. Sarkar, S. Dey, and A. Narayan, Non-Hermitian topological phases: Principles and prospects, *J. Phys.: Condens. Matter* **35**, 333001 (2023).
- [34] L. Zhou and D.-J. Zhang, Non-Hermitian Floquet topological matter—a review, *Entropy* **25**, 1401 (2023).
- [35] S.-H. Lin, R. Dilip, A. G. Green, A. Smith, and F. Pollmann, Real- and imaginary-time evolution with compressed quantum circuits, *PRX Quantum* **2**, 010342 (2021).
- [36] P. Kos, B. Bertini, and T. Prosen, Correlations in perturbed dual-unitary circuits: Efficient path-integral formula, *Phys. Rev. X* **11**, 011022 (2021).
- [37] P. W. Claeys and A. Lamacraft, Ergodic and nonergodic dual-unitary quantum circuits with arbitrary local Hilbert space dimension, *Phys. Rev. Lett.* **126**, 100603 (2021).
- [38] M. Ippoliti and V. Khemani, Postselection-free entanglement dynamics via spacetime duality, *Phys. Rev. Lett.* **126**, 060501 (2021).
- [39] B. Bertini, K. Klobas, V. Alba, G. Lagnese, and P. Calabrese, Growth of Rényi entropies in interacting integrable models and the breakdown of the quasiparticle picture, *Phys. Rev. X* **12**, 031016 (2022).
- [40] G. Kells, D. Meidan, and A. Romito, Topological transitions in weakly monitored free fermions, *SciPost Phys.* **14**, 031 (2023).
- [41] O. Alberton, M. Buchhold, and S. Diehl, Entanglement transition in a monitored free-fermion chain: From extended criticality to area law, *Phys. Rev. Lett.* **126**, 170602 (2021).
- [42] S. Gopalakrishnan and M. J. Gullans, Entanglement and purification transitions in non-Hermitian quantum mechanics, *Phys. Rev. Lett.* **126**, 170503 (2021).
- [43] P. Calabrese and J. Cardy, Evolution of entanglement entropy in one-dimensional systems, *J. Stat. Mech.* (2005) P04010.
- [44] V. Alba and P. Calabrese, Entanglement and thermodynamics after a quantum quench in integrable systems, *Proc. Natl. Acad. Sci. USA* **114**, 7947 (2017).
- [45] T. E. Lee and C.-K. Chan, Heralded magnetism in non-Hermitian atomic systems, *Phys. Rev. X* **4**, 041001 (2014).
- [46] Y. Ashida and M. Ueda, Full-counting many-particle dynamics: Nonlocal and chiral propagation of correlations, *Phys. Rev. Lett.* **120**, 185301 (2018).
- [47] A. Mostafazadeh, Pseudo-Hermiticity versus PT-symmetry III: Equivalence of pseudo-Hermiticity and the presence of antilinear symmetries, *J. Math. Phys.* **43**, 3944 (2002).
- [48] Y. Le Gal, X. Turkeshi, and M. Schiró, Volume-to-area law entanglement transition in a non-Hermitian free fermionic chain, *SciPost Phys.* **14**, 138 (2023).
- [49] G. Piccitto, A. Russomanno, and D. Rossini, Entanglement transitions in the quantum Ising chain: A comparison between different unravelings of the same Lindbladian, *Phys. Rev. B* **105**, 064305 (2022).
- [50] X. Turkeshi, M. Dalmonte, R. Fazio, and M. Schiró, Entanglement transitions from stochastic resetting of non-Hermitian quasiparticles, *Phys. Rev. B* **105**, L241114 (2022).
- [51] X. Turkeshi and M. Schiró, Entanglement and correlation spreading in non-Hermitian spin chains, *Phys. Rev. B* **107**, L020403 (2023).
- [52] C. Zerba and A. Silva, Measurement phase transitions in the no-click limit as quantum phase transitions of a non-Hermitian vacuum, [arXiv:2301.07383](https://arxiv.org/abs/2301.07383).
- [53] A. Paviglianiti and A. Silva, Multipartite entanglement in the measurement-induced phase transition of the quantum Ising chain, [arXiv:2302.06477](https://arxiv.org/abs/2302.06477).
- [54] M. Thakurathi, A. A. Patel, D. Sen, and A. Dutta, Floquet generation of Majorana end modes and topological invariants, *Phys. Rev. B* **88**, 155133 (2013).
- [55] D. J. Yates, F. H. L. Essler, and A. Mitra, Almost strong $(0, \pi)$ edge modes in clean interacting one-dimensional Floquet systems, *Phys. Rev. B* **99**, 205419 (2019).
- [56] T. Kitagawa, E. Berg, M. Rudner, and E. Demler, Topological characterization of periodically driven quantum systems, *Phys. Rev. B* **82**, 235114 (2010).
- [57] A. C. Potter, T. Morimoto, and A. Vishwanath, Classification of interacting topological Floquet phases in one dimension, *Phys. Rev. X* **6**, 041001 (2016).
- [58] D. V. Else and C. Nayak, Classification of topological phases in periodically driven interacting systems, *Phys. Rev. B* **93**, 201103(R) (2016).
- [59] B. Zeng, X. Chen, D.-L. Zhou, and X.-G. Wen, *Quantum Information Meets Quantum Matter* (Springer, Berlin, 2019).
- [60] P. Fromholz, G. Magnifico, V. Vitale, T. Mendes-Santos, and M. Dalmonte, Entanglement topological invariants for one-dimensional topological superconductors, *Phys. Rev. B* **101**, 085136 (2020).
- [61] X. Cao, A. Tilloy, and A. D. Luca, Entanglement in a fermion chain under continuous monitoring, *SciPost Phys.* **7**, 024 (2019).
- [62] L. Fidkowski, J. Haah, and M. B. Hastings, How dynamical quantum memories forget, *Quantum* **5**, 382 (2021).
- [63] P. Fendley, Strong zero modes and eigenstate phase transitions in the XYZ/interacting Majorana chain, *J. Phys. A: Math. Theor.* **49**, 30LT01 (2016).
- [64] D. J. Yates, A. G. Abanov, and A. Mitra, Dynamics of almost strong edge modes in spin chains away from integrability, *Phys. Rev. B* **102**, 195419 (2020).
- [65] X. Mi *et al.*, Noise-resilient edge modes on a chain of superconducting qubits, *Science* **378**, 785 (2022).
- [66] P. Calabrese and J. Cardy, Entanglement entropy and conformal field theory, *J. Phys. A: Math. Theor.* **42**, 504005 (2009).
- [67] W. Berdanier, M. Kolodrubetz, S. Parameswaran, and R. Vasseur, Floquet quantum criticality, *Proc. Natl. Acad. Sci. USA* **115**, 9491 (2018).

- [68] V. Alba and F. Carollo, Spreading of correlations in Markovian open quantum systems, *Phys. Rev. B* **103**, L020302 (2021).
- [69] F. Carollo and V. Alba, Dissipative quasiparticle picture for quadratic Markovian open quantum systems, *Phys. Rev. B* **105**, 144305 (2022).
- [70] G. Vidal and R. F. Werner, Computable measure of entanglement, *Phys. Rev. A* **65**, 032314 (2002).
- [71] E. J. Bergholtz, J. C. Budich, and F. K. Kunst, Exceptional topology of non-Hermitian systems, *Rev. Mod. Phys.* **93**, 015005 (2021).
- [72] X. Mi *et al.*, Stable quantum-correlated many body states via engineered dissipation, [arXiv:2304.13878](https://arxiv.org/abs/2304.13878).
- [73] B. Kraus, H. P. Büchler, S. Diehl, A. Kantian, A. Micheli, and P. Zoller, Preparation of entangled states by quantum Markov processes, *Phys. Rev. A* **78**, 042307 (2008).
- [74] F. Verstraete, M. M. Wolf, and J. Ignacio Cirac, Quantum computation and quantum-state engineering driven by dissipation, *Nat. Phys.* **5**, 633 (2009).
- [75] P. M. Harrington, E. J. Mueller, and K. W. Murch, Engineered dissipation for quantum information science, *Nat. Rev. Phys.* **4**, 660 (2022).